

High-Energy Gamma-Ray Emission from Isolated Stellar-Mass Black Hole Magnetospheres

Koki Kin,^{a,*} Shota Kisaka,^b Kenji Toma,^{a,c} Shigeo S. Kimura^{a,c} and Amir Levinson^d

^a*Astronomical Institute, Graduate School of Science, Tohoku University,
980-8578, Sendai, Japan*

^b*Physics Program, Graduate School of Advanced Science and Engineering, Hiroshima University,
739-8526, Higashi-Hiroshima, Japan*

^c*Frontier Research Institute for Interdisciplinary Sciences, Tohoku University,
980-8578, Sendai, Japan*

^d*The Raymond and Beverly Sackler, School of Physics and Astronomy, Tel Aviv University,
69978, Tel Aviv, Israel*

E-mail: koki.kin@astr.tohoku.ac.jp

In light of recent studies that show efficient particle acceleration and consequent gamma-ray emission in the magnetosphere around the supermassive black holes (SMBHs), we can expect gamma-ray emission from isolated stellar-mass BH (IBH) magnetospheres formed by accretion of interstellar medium (ISM), as well. In this work, we perform one-dimensional general relativistic particle-in-cell simulations of the IBH magnetosphere. We find that a strong electric field intermittently emerges and particles are efficiently accelerated, similarly as SMBH cases. We also build a semi-analytic model of the plasma dynamics and the photon transfer, which can explain the simulation results. Based on this model, we show that the resultant gamma rays are detectable with the *Fermi* Large Area Telescope and the Cherenkov Telescope Array, when nearby IBHs are embedded in dense gas clouds. Gamma-ray luminosity is strongly dependent on the disk property and the electric current flowing in the magnetosphere. For more details, see our published paper [1].

*High Energy Phenomena in Relativistic Outflows VIII (HEPROVIII)
23-26 October, 2023
Paris, France*

*Speaker

1. Introduction

Hundreds of millions of isolated stellar-mass black holes (IBHs) in the Galaxy are believed to remain undetected. They draw considerable attention as candidates for unidentified sources of *Fermi* Large Area Telescope (LAT) and galactic PeV energy cosmic-ray accelerators [2]. The possibility of interstellar medium (ISM) accretion onto IBHs with an efficient accumulation of the magnetic flux has been proposed by several studies (e.g., [3]). The magnetic field at the IBH vicinity can be strong enough for their accretion disks to become a highly-magnetized state (MAD; [4, 5]), and magnetospheres can be formed for such IBH-MADs [6].

Recently, several general relativistic particle-in-cell (GRPIC) simulations of super-massive BH (SMBH) magnetosphere have been conducted (e.g., [7–11]). They have observed the longitudinal electric field intermittently developing in the magnetosphere, in the case that the plasma supply to the system is insufficient to achieve a steady force-free state of the system. In such region, i.e., spark gaps, plasma particles are efficiently accelerated and escaping gamma-ray emission can be as bright as $\sim 1\%$ of the Blandford-Znajek (BZ) luminosity (c.f. [12]).

Similar spark gap may arise in charge-starved magnetospheres around IBHs during the ISM accretion, which are the source candidates of unidentified gamma-ray objects [13]. Because of the difference in the size of the system, the magnetic field strength, and the characteristics of soft photons from the MAD accretion disk between SMBH magnetospheres and that of stellar-mass BH, the plasma dynamics in the stellar-mass BH magnetospheres should be examined separately, and a numerical approach will be suitable for investigating a highly time-dependent nature of spark gap.

In the present paper we examine the dynamics of a local spark gap in the stellar-mass BH magnetosphere and the subsequent radiation characteristics, by using 1D GRPIC simulations.¹ We broadly explore the dependence of the gap activity on the ambient disk photon characteristics and the magnetospheric current (Section 3). Furthermore, we construct a semi-analytic model of particle acceleration and radiation processes in the gap which reproduces the maximum particle energies and the peak gamma-ray luminosities in the simulations. We demonstrate the spectra of escaping gamma-rays in some cases by using this model (Section 4), and briefly discuss the detectability (Section 5).

2. The Numerical Simulation

We use the 1D GRPIC code described in [7, 10, 11] (hereafter LC18, K20 and K22). Under the assumption that the gap activity does not affect global magnetic structure, we solve the Maxwell's equations for the longitudinal electric field E_r measured in the frame of a zero angular momentum observer (ZAMO) in a background Kerr spacetime, given in Boyer-Lindquist coordinates (see Appendix),

$$\partial_r \left(\sqrt{A} E_r \right) = 4\pi \Sigma (j^t - \rho_{\text{GJ}}), \quad (1)$$

and

$$\partial_t \left(\sqrt{A} E_r \right) = -4\pi (\Sigma j^r - J_0), \quad (2)$$

¹Although 2D simulations (e.g., [8, 9]) can provide more complete analysis on the global magnetospheric structure, they cannot resolve the skin depth for realistic conditions and require proper rescaling that needs to be better assessed.

where A and Σ is metric components defined in Eq. (10), j^t and j^r the charge and the current density. ρ_{GJ} denotes the Goldreich-Julian (GJ) charge density, and J_0 the magnetospheric current parameterized by $J_0 = j_0 \omega_{\text{H}} B_{\text{H}} / 4\pi (r_{\text{H}}^2 + a^2) \cos \theta$, where B_{H} denotes the magnetic field strength at the horizon, $r_{\text{H}} = r_{\text{g}} (1 + \sqrt{1 - a_*^2})$ the horizon radius ($r_{\text{g}} = GM/c^2$ the gravitational radius of the BH with mass M), $\omega_{\text{H}} = a_* c / 2r_{\text{H}}$ the angular velocity of the BH ($a_* \equiv a/r_{\text{g}}$ is the dimensionless spin parameter). $j_0 = -1$ corresponds to the magnetospheric current in the BZ force-free solution where the current flows inwards except for the equatorial plane. We simultaneously solve the equation of motion for electrons and positrons, which is

$$\frac{du_i}{dt} = -\sqrt{g^{\text{tr}}} \gamma_i \partial_r(\alpha) + \alpha \left(\frac{q_i}{m_e} E_r - \frac{P_{\text{cur}}(\gamma_i)}{m_e v_i} \right), \quad (3)$$

where α is the lapse function (Eq. (9)), q_i the charge of i th particle, $u_i = \sqrt{g_{\text{tr}}} u_i^t$ the normalized four-velocity component in the r direction measured by a ZAMO, γ_i the Lorentz factor, $v_i = u_i / \gamma_i$ the three-velocity component, and $P_{\text{cur}}(\gamma_i) = 2e^2 \gamma_i^4 v_i / 3r_{\text{g}}^2$ the curvature power with the curvature radius fixed as r_{g} . Photons are treated as charge-neutral particles in the calculations. The null geodesic equation for them is

$$\frac{d\tilde{p}_j^r}{dt} = -\sqrt{g^{\text{tr}}} \tilde{p}_j^t \partial_r(\alpha), \quad (4)$$

where \tilde{p}_j^μ ($\mu = t, r$) is the momentum components of j th photon measured by a ZAMO.

We consider inverse Compton (IC) scattering of soft photons from the accretion disk and $\gamma\gamma$ pair production by the scattered photons and the soft photons by using the Monte-Carlo approach: In each time step, we evaluate the probability of these interactions for all particles in the simulating region. If a IC scattering event occurs, then we add a newly-created IC photon in the calculations, and reduce the scattering particle's energy correspondingly. If an annihilation event occurs, then we erase the interacting photon and add one e^+e^- pair to the calculations. The intensity of the soft photon field is assumed to be steady, isotropic, and homogeneous with a simple power-law spectrum $I_s(\epsilon_s) = I_0 (\epsilon_s / \epsilon_{\text{min}})^{-p}$ ($\epsilon_{\text{min}} \leq \epsilon_s \leq \epsilon_{\text{max}}$), where ϵ_s is the soft photon energy normalized by the electron rest mass energy $m_e c^2$. The fiducial optical depth τ_0 is related to the intensity normalization I_0 as $\tau_0 = n_s(\epsilon_{\text{min}}) \sigma_{\text{T}} r_{\text{g}} = 4\pi \sigma_{\text{T}} r_{\text{g}} I_0 / hc$, where σ_{T} is the Thomson cross section and h is the Planck constant.

We apply this model to a BH with $M = 10M_{\odot}$ and $a_* = 0.9$. The computational domain is set from $r_{\text{min}} \simeq 1.5r_{\text{g}}$ to $r_{\text{max}} \simeq 4.3r_{\text{g}}$. We impose the open boundary condition for both boundaries. The inclination of the simulating region to the BH rotation axis is set as $\theta = 30^\circ$. We set $B_{\text{H}} = 2\pi \times 10^7$ G in the present work, where we implicitly assume the accretion disk to be a MAD state with sub-Eddington mass accretion rate $\dot{M} \sim 10^{-3} \dot{M}_{\text{Edd}}$ ($\dot{M}_{\text{Edd}} \equiv 4\pi GMm_{\text{p}} / \sigma_{\text{T}} c$), likewise K20, K22. We change p , ϵ_{min} , τ_0 , and j_0 for each simulating runs to investigate the dependence of the gap activity on the soft photon characteristics and the magnetospheric current. A fiducial value of the peak energy, $\epsilon_{\text{min}} = 10^{-6}$, which is consistent with the calculation of photon spectra from IBH-MADs (see [3]).

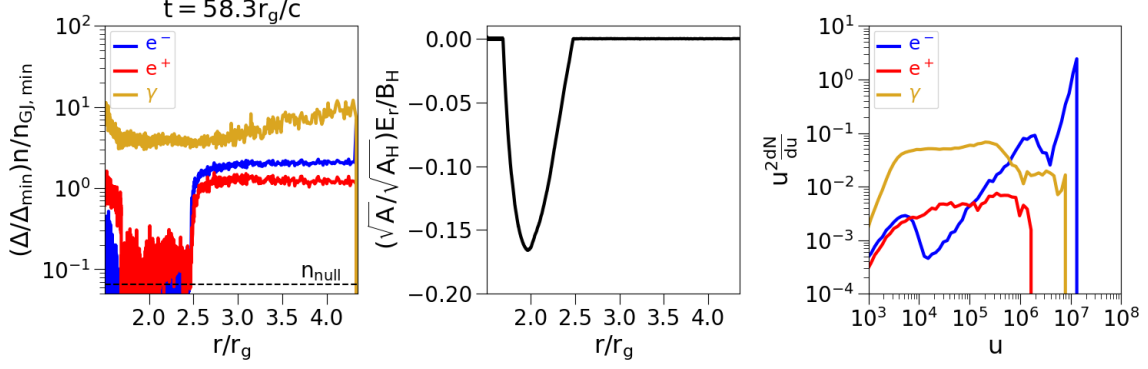


Figure 1: A snapshot of the gap at the peak time of the electric field development ($t = 58.3r_g/c$) in model LA1. The three panels from *left to right* are (1) the number density of each particle species normalized by the GJ number density at the simulation inner boundary $n_{\text{GJ}, \text{min}} = \rho_{\text{GJ}, \text{min}}/e$ (Δ is the metric component (Eq. (10)), $\Delta_{\min} = \Delta(r_{\min})$), (2) the electric field distribution normalized by B_H , and (3) the energy distribution of outgoing particles of each species.

3. Simulation Results

In the simulations, we observe a quasi-steady, or quasi-periodic development of E_r with a timescale $t \lesssim 10r_g/c$ for $\tau_0 \geq 30$,² similar to K20 and K22. The charge deficiency around the null charge surface r_{null} (where $\rho_{\text{GJ}} = 0$, $r_{\text{null}} \approx 2.0$ for $a_* = 0.9$) is induced by inward and outward drifts of plasma, and the electric field E_r develops according to Eqs. (1) and (2). During the peak time of E_r amplitude (see Fig. 1), electrons are accelerated up to $u \sim \gamma_e \sim 10^7$ and scatter disk soft photons. Those photons annihilate with other soft photons to produce pairs and compensate the charge depletion. Accelerated particles will also produce high energy gamma-rays via the curvature process. The peak luminosities are $L_{\text{cur}, \text{pk}} \sim 10^{-2}L_{\text{BZ}}$ for the curvature process and $L_{\text{ic}, \text{pk}} \sim 10^{-4}L_{\text{BZ}}$ for IC scattering, where $L_{\text{BZ}} = (\kappa_{\text{B}}/4\pi c)\omega_{\text{H}}^2\Phi_{\text{H}} = (\kappa_{\text{B}}\pi c/4)a_*^2B_{\text{H}}^2r_g^2$ is the BZ luminosity ($\kappa_{\text{B}} \sim 0.053$ for the split-monopole magnetic field configuration, see [14]).

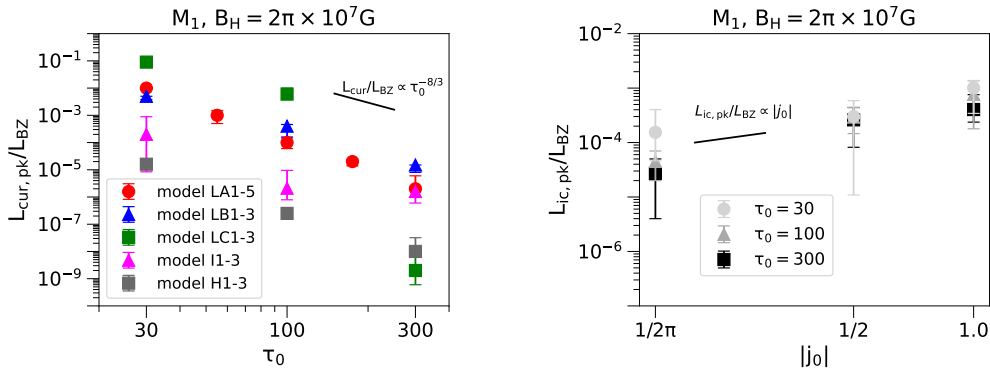


Figure 2: Plots of the peak curvature luminosities normalized by L_{BZ} (*left*) in our simulations with various values of p , ϵ_{\min} , and j_0 as functions of τ_0 and the peak IC luminosities normalized by L_{BZ} (*right*) in our simulations with $\epsilon_{\min} = 10^{-6}$ and $p = 2.0$ as functions of $|j_0|$.

²For $\tau_0 = 10$, the simulation box slowly approaches the vacuum state with all the three j_0 values, which is also consistent with what we saw in K20.

Fig. 2 shows the ratio of the curvature/IC peak luminosities to the BZ luminosity as a function of τ_0 for $\{p, \epsilon_{\min}, j_0\} = \{2.0, 10^{-6}, -1/2\pi\}$ (model LA1-5), $\{2.5, 10^{-6}, -1/2\pi\}$ (LB1-3), $\{2.0, 10^{-5}, -1/2\pi\}$ (LC1-3), $\{2.0, 10^{-6}, -1/2\}$ (I1-3), and $\{2.0, 10^{-6}, -1\}$ (H1-3). The luminosity difference seen here reflects the dynamical difference of the gap for each models: Varying the peak energy of seed photon spectrum ϵ_{\min} yields larger gap for $\tau_0 \lesssim 100$, thus the peak curvature luminosity is ~ 10 times higher than their lower ϵ_{\min} counterparts. This is because most of the IC scatterings occur in Klein-Nishina (KN) regime, for which the pair production optical depth is independent on p , but dependent on ϵ_{\min} (see K20). For higher values of the global magnetospheric current j_0 , we observe much lower amplitudes of E_r , because the plasma density around the null surface $n(r_{\text{null}})$ become higher for larger $|j_0|$ in order to satisfy Eq. (2) everywhere. A rough scaling relation for $n(r_{\text{null}})$ during the peak time is $(\Delta(r_{\text{null}})/\Delta(r_{\text{min}}))(n(r_{\text{null}})/n_{\text{GJ,min}}) \sim -0.58j_0$. Correspondingly, $L_{\text{cur,pk}}$ declines, due to the sensitive dependence of the curvature power on γ_e ($P_{\text{cur}} \propto \gamma_e^4$). $L_{\text{ic,pk}}$ is, on the other hand, roughly scaled as $L_{\text{ic,pk}} \propto |j_0|$, since the scattering particles in the gap increases with $|j_0|$.

4. Gamma-Ray Signals from Isolated Stellar-Mass BHs

4.1 Semi-Analytic Model of The Gap

We have seen quasi-periodic/steady behaviors of the gap similarly as SMBH cases (K20, K22). This similarity motivate us to construct a semi-analytic model applicable over the wide range of masses M and accretion rates \dot{M} . We firstly evaluate the input parameters of the semi-analytic model, ϵ_{\min} , τ_0 , and B_{H} , by using the one-zone MAD model of [3], in which \dot{M} is assumed to be the Bondi-Hoyle-Lyttleton accretion rate, $\dot{M} \simeq 10^{14} M_1^2 n_{\text{ISM},2} \text{ g s}^{-1}$. We consider thermal synchrotron emission from the MAD as the seed photons for IC scatterings and $\gamma\gamma$ pair productions in the gap, so that ϵ_{\min} and τ_0 is

$$\epsilon_{\min} = x_{\text{M}} \frac{3}{4\pi} \frac{heB}{m_e^2 c^3} \theta_e^2 \simeq 3.8 \times 10^{-6} \left(\frac{x_{\text{M}}}{25}\right) M_1^{-1} n_{\text{ISM},2}^{-1/2} \mathcal{R}_1^{-1/4} \alpha_{-0.5}^{3/2} \beta_{-1}^{1/2}, \quad (5)$$

and

$$\tau_0 = \frac{4\pi}{c} \frac{\nu_{\text{syn,pk}} L_{\nu_{\text{syn,pk}}}}{4\pi^2 R^2 \epsilon_{\min} m_e c^2} \sigma_{\text{T}} r_{\text{g}} \simeq 38 M_1^2 n_{\text{ISM},2}^{3/2} \mathcal{R}_1^{-7/4} \alpha_{-0.5}^{-3/2} \beta_{-1}^{-1/2}, \quad (6)$$

where $\theta_e = k_{\text{B}} T_e / m_e c^2$ denotes the normalized electron temperature determined by the energy balance in MAD, $R = \mathcal{R} r_{\text{g}}$ the size of MAD, B the magnetic field of MAD, and x_{M} a numerical factor ($x_{\text{M}} \sim 25$ for the synchrotron-self-absorption thin limit). $\nu_{\text{syn,pk}}$ and $L_{\nu_{\text{syn,pk}}}$ are the synchrotron peak frequency and specific luminosity.³ B_{H} is calculated as $B_{\text{H}} = \phi_{\text{BH}} (\dot{M} c)^{1/2} / 2\pi r_{\text{g}} \simeq 1.1 \times 10^7 (\phi_{\text{BH}}/50) M_1^{-1} \dot{M}_{14}^{1/2} \text{ G}$ ([14]).

We then calculate energy evolution of the outgoing electron from the inner boundary of the gap r_{in} . Eq. (3) can be rewritten for ultra-relativistic electrons (for which $\alpha c dt \approx \sqrt{g_{\text{tr}}} dr$) as

$$\frac{d\gamma_e}{dr} = -\frac{\sqrt{g_{\text{tr}}}}{m_e c^3} [e E_r(r, r_{\text{in}}, B_{\text{H}}) c + P_{\text{cur}}(\gamma_e) + P_{\text{ic}}(\gamma_e)], \quad (7)$$

³Here and hereafter we use the convention $Q_x = (Q/10^x)$ in cgs units, except for the BH mass, $M = 10^x M_{\text{X}} M_{\odot}$.

where we have added the IC cooling term P_{ic} in the equation. E_r is obtained from the vacuum ($j^t = 0$) solution of Eq. (1) with the boundary condition $E_r(r_{in}) = 0$. In each step, we calculate γ_e , IC scattered photon's energy ϵ_{ic} , and the IC mean free path l_{ic} to evaluate IC photons produced in each step $\delta N_\gamma = dr/l_{ic}$. Then, we assume that all of them will convert to pairs at the 'pair production front' $r_{ppf} = r + l_{\gamma\gamma}$, where $l_{\gamma\gamma}$ is the $\gamma\gamma$ mean free path. In this manner, we iterate the amount of pairs produced by one electron propagating through $[r_{in}, r]$, $N_{pair}(r) = \sum_{r_{ppf} \leq r} \delta N_{pair}(r_{ppf})$. The gap outer boundary r_{out} is determined by criteria $N_{pair}(r_{out}) = \pi/|j_0|$ and $\xi(r_{out}) + \xi(r_{in})/2 = \xi(r_{null})$,⁴ which are set to match the simulation results. Finally, $\gamma_{e,max} = \max\{\gamma_e(r; r_{in} \leq r \leq r_{out})\}$, $L_{cur,pk} = \int_{r_{in}}^{r_{out}} \alpha^2 P_{cur}(\gamma_e(r)) n(r_{null}) \Sigma dr$, and $L_{ic,pk} = 10^{-4} |j_0| L_{BZ}$.

4.2 Spectral Calculation

In Fig. 3, we show the emission spectra from IBH-MADs with magnetospheric gaps for two reference parameters, $M = 10M_\odot$, $n_{ISM} = 100 \text{ cm}^{-3}$ and $M = 50M_\odot$, $n_{ISM} = 10 \text{ cm}^{-3}$. As can be seen, gap gamma-ray spectra have a peak around GeV-TeV energy band, which corresponds to the detectable energy range of *Fermi*-LAT and Cherenkov Telescope Array. The luminosity is higher for $j_0 = -1/2\pi$, owing to the efficient curvature radiation. For $j_0 = -1/2$, the curvature peak luminosity and the characteristic frequency are $10^2 - 10^3$ times lower than those for $j_0 = -1/2\pi$, but IC emission is dominant in the GeV-TeV energy band due to the scaling $L_{ic,pk} \propto |j_0|$ (see Section. 3). Considering the achieved luminosity $L \gtrsim 10^{31} \text{ erg s}^{-1}$, we can expect the gamma-ray signals from gaps of stellar-mass BHs embedded in dense gas clouds located at the distances $\sim \text{kpc}$ are bright enough for the detection.

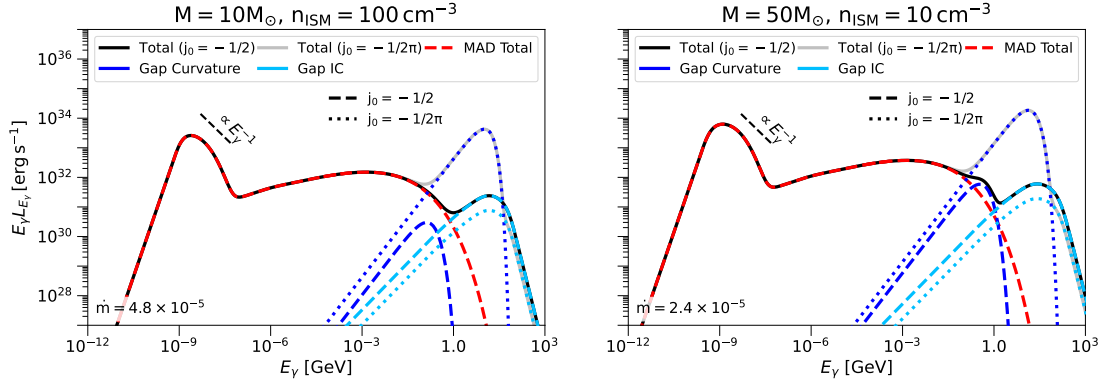


Figure 3: Broadband emission spectra from IBH-MADs with magnetospheric gaps in cases of $M = 10M_\odot$, $n_{ISM} = 100 \text{ cm}^{-3}$ (left) and $M = 50M_\odot$, $n_{ISM} = 10 \text{ cm}^{-3}$ (right). The value of $\dot{m} = \dot{M}/\dot{M}_{Edd}$ is shown in each panel. The black and gray solid lines represent the total emission for $j_0 = -1/2$ and $j_0 = -1/2\pi$, respectively. The red dashed line represents radiation from the MAD, which consists of synchrotron radiation from the MAD thermal electrons (which forms the humps in the optical band) and that from the MAD non-thermal electrons. Spectra of the curvature and IC radiation from the gap are shown by the blue and light-blue lines, respectively. For each of them, the dashed lines correspond to those for $j_0 = -1/2$ case and the dotted ones for $j_0 = -1/2\pi$ case.

⁴ ξ denotes the tortoise coordinate, described as $\xi = \ln[(r - r_+)/ (r - r_-)] / (r_+ - r_-)$, where $r_\pm = (1 \pm \sqrt{1 - a_*^2})$.

5. Summary and Discussion

We have conducted a comprehensive investigation of the dynamics of spark gaps in charge-starved magnetospheres of stellar-mass Kerr BHs, using the 1D GRPIC code described in LC18, K20, and K22. Differences of dynamics for changing spectral properties of seed photons and the magnetospheric current have been examined. We have also constructed semi-analytic model reproducing the simulation results, and have estimated the gamma-ray emission characteristics from IBHs. Gamma-ray signals from IBH magnetospheric gaps embedded in the dense gas clouds at the distances \sim kpc are suggested to be bright enough for detection in the GeV-TeV energy band.

Expected main targets are *Fermi*-LAT unidentified objects. Candidates can be distinguished by a hard spectral index ($\Gamma \sim 2/3$) with a break around the GeV-TeV and a point-source like morphology. The optical signals from the MADs resembles that from white dwarfs [3], which can be found by *Gaia*, and the MAD X-ray signals can be detected by X-ray observations including eROSITA and ROSAT. Thus, we could specify our IBH candidates by examining associations among *Fermi*-LAT unIDs, X-ray sources, and *Gaia* white-dwarf-like objects.

Our 1D calculations do not take account of a general relativistic lensing effect on the photon transfer. This affects the light curve, which will be considered in the future work. Differences between 1D and 2D GRPIC simulation results on the gap dynamics (for example, see [9]) should also be further investigated. We have shown that J_0 (or the toroidal magnetic field) substantially affects the gap dynamics. The toroidal field is determined by external pressure on the magnetosphere. Including effects of variable external pressure in 2D simulations would be interesting.

Appendix

Spacetime

The Kerr metric is given in Boyer-Lindquist coordinates as

$$ds^2 = -\alpha^2 dt^2 + g_{\phi\phi} (d\phi - \omega dt)^2 + g_{rr} dr^2 + g_{\theta\theta} d\theta^2, \quad (8)$$

where

$$\alpha^2 = \frac{\Sigma\Delta}{A}, \quad \omega = \frac{2ar_g r}{A}, \quad g_{rr} = \frac{\Sigma}{\Delta}, \quad g_{\theta\theta} = \Sigma, \quad g_{\phi\phi} = \frac{A}{\Sigma} \sin^2 \theta, \quad (9)$$

with

$$\Delta = r^2 + a^2 - 2r_g r, \quad \Sigma = r^2 + a^2 \cos^2 \theta, \quad A = (r^2 + a^2)^2 - a^2 \Delta \sin^2 \theta. \quad (10)$$

References

- [1] Kin, K., Kisaka, S., Toma, K., Kimura, S. S., & Levinson, A., *1D GRPIC Simulations of Stellar-Mass Black Hole Magnetospheres: Semi-Analytic Model of Gamma-Rays from Gaps*, *ApJ* **964** (2024) 78
- [2] Ioka, K., Matsumoto, T., Teraki, Y., Kashiya, K., & Murase, K., *GW 150914-like black holes as Galactic high-energy sources*, *MNRAS* **470** (2017) 3332

- [3] Kimura, S. S., Kashiyama, K., & Hotokezaka, K., *Multiwavelength Emission from Magnetically Arrested Disks around Isolated Black Holes*, *ApJL* **922** (2021) L15
- [4] Narayan, R., Igumenshchev, I. V., & Abramowicz, M. A., *Magnetically Arrested Disk: an Energetically Efficient Accretion Flow*, *PASJ* **55** (2003) L69
- [5] McKinney, J. C., Tchekhovskoy, A., & Blandford, R. D., *General relativistic magnetohydrodynamic simulations of magnetically choked accretion flows around black holes*, *MNRAS* **423** (2012) 3083
- [6] Kaaz, N., Murguia-Berthier, A., Chatterjee, K., Liska, M. T. P., & Tchekhovskoy, A., *Jet Formation in 3D GRMHD Simulations of Bondi-Hoyle-Lyttleton Accretion*, *ApJ* **950** (2023) 31
- [7] Levinson, A., & Cerutti, B., *Particle-in-cell simulations of pair discharges in a starved magnetosphere of a Kerr black hole*, *A&A* **616** (2018) A184
- [8] Parfrey, K., Philippov, A., & Cerutti, B., *First-Principles Plasma Simulations of Black-Hole Jet Launching*, *PhRvL* **122** (2019) 035101
- [9] Crinquand, B., Cerutti, B., Philippov, A., Parfrey, K., & Dubus, G., *Multidimensional Simulations of Ergospheric Pair Discharges around Black Holes*, *PhRvL* **124** (2020) 145101
- [10] Kisaka, S., Levinson, A., & Toma, K., *Comprehensive Analysis of Magnetospheric Gaps around Kerr Black Holes Using 1D GRPIC Simulations*, *ApJ* **902** (2020) 80
- [11] Kisaka, S., Levinson, A., Toma, K., & Niv, I., *The Response of Black Hole Spark Gaps to External Changes: A Production Mechanism of Rapid TeV Flares?*, *ApJ* **924** (2022) 28
- [12] Blandford, R. D., & Znajek, R. L., *Electromagnetic extraction of energy from Kerr black holes*, *MNRAS* **179** (1977) 433
- [13] Hirotani, K., Pu, H.-Y., Outmani, S., et al., *High-energy and Very High Energy Emission from Stellar-mass Black Holes Moving in Gaseous Clouds*, *ApJ* **867** (2018) 120
- [14] Tchekhovskoy, A., Narayan, R., & McKinney, J. C., *Black Hole Spin and The Radio Loud/Quiet Dichotomy of Active Galactic Nuclei*, *ApJ* **711** (2010) 50